The Astrophysical Journal Letters, 955:L20 (11pp), 2023 September 20 https://doi.org/10.3847/2041-8213/acf857

Fundamental–Harmonic Pairs of Interplanetary Type III Radio Bursts

Immanuel Christopher Jebaraj[1], Vladimir Krasnoselskikh[2,3], Marc Pulupa[3], Jasmina Magdalenic[4,5], and Stuart D. Bale[3,6]
[1] Space Research Laboratory, University of Turku, Turku, Finland; immanuel.c.jebaraj@gmail.com
[2] LPC2E/CNRS, UMR 7328, 3A Avenue de la Recherche Scientifique, Orleans, France
[3] Space Sciences Laboratory, University of California, Berkeley, CA 94720-7450, USA
[4] Center for Mathematical Plasma Astrophysics, Department of Mathematics, KU Leuven, Celestijnenlaan 200B, B-3001 Leuven, Belgium
[5] Solar-Terrestrial Centre of Excellence—SIDC, Royal Observatory of Belgium, Avenue Circulaire 3, B-1180 Uccle, Belgium
[6] Physics Department, University of California, Berkeley, CA 94720-7300, USA
Received 2023 April 26; revised 2023 September 8; accepted 2023 September 10; published 2023 September 21

Abstract

Type III radio bursts are not only the most intense but also the most frequently observed solar radio bursts. However, a number of their defining features remain poorly understood. Observational limitations, such as a lack of sufficient spectral and temporal resolution, have hindered a full comprehension of the emission process, especially in the hectokilometric wavelengths. Of particular difficulty is the ability to detect the harmonics of type III radio bursts. Here we report the first detailed observations of type III fundamental–harmonic pairs in the hectokilometric wavelengths, observed by the Parker Solar Probe. We present a statistical analysis of the spectral characteristics and polarization measurements of the fundamental–harmonic pairs. Additionally, we quantify various characteristics of the fundamental–harmonic pairs, such as the time delay and time profile asymmetry. Our report concludes that fundamental–harmonic pairs constitute a majority of all type III radio bursts observed during close encounters when the probe is in close proximity to the source region and propagation effects are less pronounced.

Unified Astronomy Thesaurus concepts: Solar radio emission (1522); Solar electromagnetic emission (1490); Interplanetary turbulence (830); Interplanetary physics (827)

1. Introduction

Type III radio bursts are the most intense and well-observed radio emissions of solar origin in the solar system. They are the radio signatures of energetic electron beams accelerated at the Sun that stream away into the heliosphere along open magnetic field lines (McLean & Melrose 1985). In the dynamic radio spectrum, which presents intensity as a function of time and frequency, type III bursts are distinguished as rapidly drifting emissions. Although various aspects of type III bursts—including their electron beam evolution, interaction with the background plasma, and subsequent electromagnetic (EM) emission—are still not entirely understood, it is generally accepted that they are generated through the plasma emission mechanism, which is a two-step process (Ginzburg & Zhelezniakov 1958; Melrose 1980, and references therein). Initially, streaming electrons interact with the background plasma, generating Langmuir waves close to the electron plasma frequency (f_p). In the second, nonlinear stage, these Langmuir waves are partially converted to EM waves by wave–wave or wave–particle interactions. The resultant EM wave is emitted close to either f_p or its harmonics (nf_p; nth harmonic of the plasma frequency, where $n = 2, 3, \ldots$; Robinson & Cairns 1998a, 1998b, 1998c).

Type III radio bursts are occasionally observed in the metric–decametric (M-D) wavelengths as distinguishable pairs of fundamental (F) and harmonic (H)[7] components. However, they have never been identified as such in the longer hectokilometric (H-K) wavelengths (see review of type III H observation difficulties in Dulk 2000). Although attempts have been made to identify the different emission components when the source of the emission was observed in situ (Kellogg 1980; Reiner & MacDowall 2019), such scarce reporting of this F phenomenon is likely due to the lack of appropriate observational capabilities. This has led to an inconsistent understanding of the plasma emission mechanism from the solar corona to interplanetary space.

For the first time, we clearly demonstrate that the most common emission configuration of type III radio bursts in the H-K wavelengths is undoubtedly as F–H pairs. Our findings were made using the observations from the FIELDS instrument suite (Bale et al. 2016) on the Parker Solar Probe (PSP; Fox et al. 2016) during its close encounters (CEs). Furthermore, radio emissions at larger distances (i.e., lower frequencies) are influenced much more by propagation effects (e.g., Krupar et al. 2020). This letter aims to provide the characteristics of type III radio bursts observed by PSP during CEs when the observer is close to the source and where the propagation effects are expected to be less pronounced.

We introduce the experimental details of the study in Section 2 and the spectral characteristics of the type III F–H pairs in Section 3. We provide additional evidence for the existence of the F–H pairs through polarization measurements in Section 4.

2. Experimental Details

In this study, we employ the remote-sensing measurements made by the radio frequency spectrometer (RFS; Pulupa et al. 2017), which combines observations from both the high-frequency receiver (HFR) and low-frequency receiver (LFR). Both receivers have an ∼4% frequency resolution. Figure 1(a) presents both the HFR and LFR measurements of a 15 minute

[7] We shall also use f_F and f_H, particularly when discussing the emission frequency of F and H.

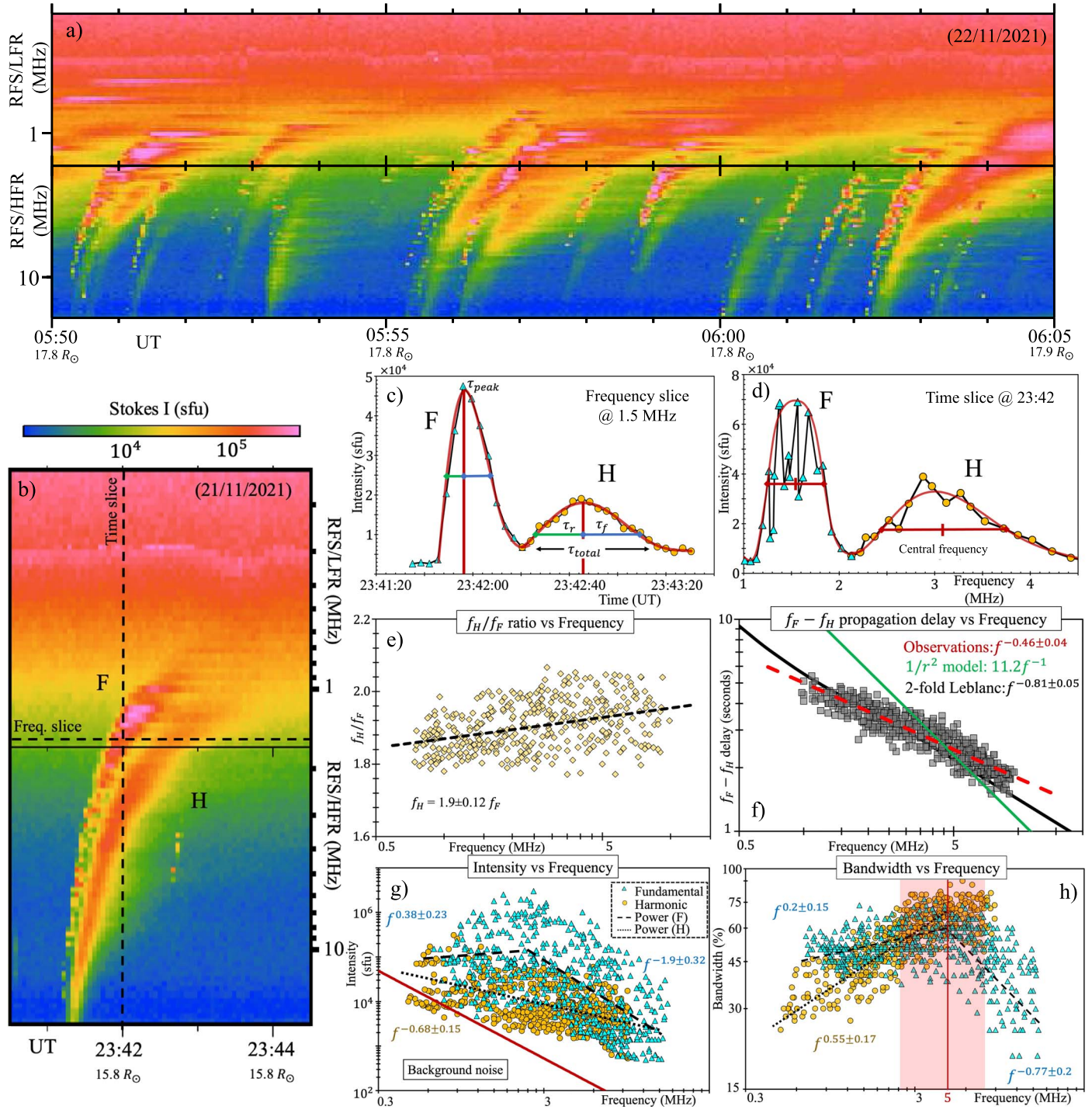

Figure 1. Statistics of spectral characteristics obtained from the analysis of 31 type III F–H pairs. Panel (a) shows a 15 minute interval on 2021 November 22 where 14 out of 17 type III bursts are F–H pairs. Panel (b) shows an example of a typical type III radio burst with F–H emission and fine structures observed on 2021 November 21. The dashed lines represent the frequency (1.5 MHz) and time (23:42 UT) slices from the spectrogram, which are presented in panels (c) and (d). In panels (a) and (b), the *x*-axis marks the observer's distance from the Sun. The data points (blue triangles for F and yellow circles for H) are fitted with an exponentially modified Gaussian (red curve). Here τ_r and τ_f are the rising and falling times, and $\tau_{\rm peak}$ is the peak intensity. The statistics of the $f_{\rm H}/f_{\rm F}$ ratio and the $f_{\rm F} - f_{\rm H}$ propagation delay as dependencies of frequency are presented in panels (e) and (f). Panels (g) and (h) present the intensity and bandwidth as a function of the frequency, respectively. The F and H are represented by the blue triangles and yellow circles. For a one-to-one comparison with F, the results of H are presented as $f_{\rm H}/2$. The average background noise (QTN + galactic) is illustrated in panel (f) by the red line, which scales as $1/f^{2.2\pm0.4}$. The vertical red line and red shaded region in panel (g) mark the peak bandwidth and its spread.

interval where a majority (14 out of 17, i.e., >80%) of the type III bursts are F–H pairs. Figure 1(b) presents a typical type III burst with F and H components during the 10th CE of PSP. We analyzed bursts observed during and after the sixth CE due to the enhanced 3.5 s temporal resolution.

We analyzed 31 type III radio bursts observed during the 6th–10th CEs of PSP; see Table 1. First, we obtained calibrated flux in units of flux density, i.e., W m^{-2} Hz^{-1} or solar flux units (sfu), following the methodology described in Page et al. (2022). Using the effective antenna length

Table 1
The 31 F–H Pairs of Type III Bursts Analyzed in This Study

Date (dd/mm/yyyy)	Start (UT)	Stop (UT)	Distance (au)
13/09/2020	18:54:40	19:08:00	0.45
26/04/2021	03:07:00	03:09:00	0.18
27/04/2021	10:23:51	10:26:00	0.13
02/05/2021	17:52:00	17:56:00	0.18
03/05/2021	15:36:50	15:42:00	0.21
08/08/2021	21:04:10	21:07:20	0.09
	16:13:10	16:15:30	0.16
18/11/2021	18:05:10	18:10:00	0.15
	20:19:20	20:21:40	0.15
21/11/2021	23:41:20	23:43:10	0.07
	23:56:00	23:57:10	0.07
	02:45:30	02:47:10	0.08
	03:30:00	03:32:15	0.08
	03:49:40	03:52:20	0.08
	04:19:40	04:21:30	0.08
	04:42:40	04:47:30	0.08
22/11/2021	06:02:10	06:06:00	0.08
	06:43:20	06:46:00	0.08
	07:03:20	07:06:00	0.08
	10:12:15	10:16:00	0.08
	11:39:20	11:41:10	0.09
	12:25:59	12:31:00	0.09
	23:30:30	23:32:00	0.11
23/11/2021	08:58:30	09:00:30	0.13
	12:35:25	12:36:40	0.14
24/11/2021	11:08:05	11:09:30	0.18
	13:52:10	13:54:00	0.18
	01:35:45	01:38:30	0.23
26/11/2021	07:35:15	07:38:30	0.24
	20:29:50	20:31:00	0.26
27/11/2021	07:48:05	07:49:50	0.28

Note. Together with the start and end times of the burst, we provide the radial distance of PSP at the time of observation. The level 2 FIELDS/RFS data (intensities are in units of power spectral density, V^2 Hz^{-1}) are open to the public and can be accessed from https://fields.ssl.berkeley.edu/data/.

($L_{\rm eff} = L_{34}/L_{12} = 0.99 \pm 0.01$), capacitive gain factor ($\Gamma = 0.32$), and impedance of free space ($Z_0 = 377\Omega$) in the following relationship from Pulupa et al. (2017), the flux density can be estimated:

$$P[V^2\mathrm{Hz}^{-1}] = S[W\mathrm{m}^{-2}\mathrm{Hz}^{-1}] \times Z_0 L_{\rm eff}^2 \Gamma^2. \quad (1)$$

To avoid potential convolutions arising from consecutive bursts, we have specifically chosen 31 isolated bursts. Our selection criterion for brightness required each burst to surpass the background level by at least 500 sfu at 15 MHz. Figure 1(g) shows the steep increase of the total background noise (solid red line) below 5 MHz. Here the level of noise is a pre-event average of the 31 bursts observed between CEs 6 and 10, and it scales close to $f^{-2.2\pm0.4}$, where f is the frequency. The presence of a standard deviation in this context is attributed to the variability of the pre-event background, which is dependent on the electron density/temperature during each specific period of the bursts. In combination with the fact that the measurements were conducted during active CEs, this may provide an explanation for the observed shallower scaling law in comparison to the one obtained by Liu et al. (2023), i.e., f^{-3}. An important point to clarify is that we did not differentiate between the quasi-thermal noise (QTN) and galactic noise. The galactic noise is frequency-dependent and can reach a maximum of 1000 sfu at close to 3 MHz (Page et al. 2022). At these frequencies corresponding to the peak of the galactic noise, the type III fluxes are typically several orders of magnitude higher.

3. Spectral Characteristics

Proximity to the Sun and the source of the radio emission provided increased sensitivity to the unique spectral features of type III radio bursts very rarely or almost never observed in the H-K wavelengths, such as striations and Hs. These features provide important findings contributing to our understanding of the nature of the plasma emission process at the H-K wavelengths. Although recent observations have reported fine structures of interplanetary type III bursts (Pulupa et al. 2020; Chen et al. 2021; Jebaraj et al. 2023b), the observations of type III F–H pairs have yet to be proven conclusively.

The PSP observations during the CEs show that a significant number of type III bursts are observed as F–H pairs, regardless of their emission intensity. To emphasize the rate of occurrence, a 15 minute time interval was randomly selected on 2021 November 22. Within this interval, it was discovered that out of the 17 type IIIs, 14 were F–H pairs, accounting for slightly over 80% (Figure 1(a)). This finding highlights that the majority of type III bursts observed in this frequency range during CEs are F–H pairs. Similarly, type III radio bursts were visually identified and included in the general statistics for the occurrence rates of F–H pairs during CEs. Only type III bursts that exceeded the background by at least 500 sfu at 15 MHz were taken into account, while bursts occurring in close proximity (more than two type III F–H pairs within a minute) were excluded to prevent signal convolution. It should be noted that large type III storms associated with eruptive events, such as those on 2021 April 26 and 2021 April 27, were not included in the statistical analysis. However, other active periods with relatively lower occurrence rates of type IIIs that still satisfied our criteria were included, such as the type III storm on 2021 November 22. In order to differentiate between occurrence rates during active periods (storm) and calmer periods (non-storm), separate statistical analyses were conducted for each. The results of this analysis are presented in Table 2. These findings provide further quantitative confirmation that a large number of the type III bursts observed during PSP CEs are F–H pairs. It is worth noting that while there was a significant occurrence of type III F–H pairs during the storms (78%), slightly lower, yet still significant, rates of occurrence were also observed during calmer periods (70%).

A customary disclaimer regarding visual identification is that it possesses certain drawbacks, including convolution from multiple type IIIs, which can appear as a single burst. In order to mitigate or substantially reduce potential errors, a rigorous methodology for F–H pair identification has been implemented. Only bursts that met the following three criteria were chosen.

1. The F–H pairs exhibit a relationship where $f_{\rm H}$ is approximately twice $f_{\rm F}$.
2. The F–H pairs are morphologically distinguishable, with F being structured and H being diffuse and smooth.
3. The polarization of the F–H pairs is morphologically distinguishable. For more information on the polarization of F–H pairs, refer to Section 4.

Table 2
Occurrence Rate of Type III Burst F–H Pairs during PSP CEs 6–10

CE	Type III Bursts	Type III F–H Pairs	Rate of Occurrence
CE 6 (NS)	4	2	50%
CE 7 (NS)	28	19	68%
CE 8 (S)	1167[a]	812	70%
(NS)	107	71	66%
CE 9 (NS)	49	32	65%
CE 10 (S)	1877	1573	84%
(NS)	142	110	77%
Total (S)	3044	2385	78%
(NS)	330	234	70%

Note. The occurrence rates during type III storms (S) and quiet periods (NS) are separated.
[a] The intense type III storm after the CME at 11:00 UT on 2021 April 26 until 16:00 UT on 2021 April 27 was not included in the statistics.

As presented in Figure 1(a), the F and H components of the type III bursts show distinct morphological features thought to be related to the different mode-conversion mechanisms (Ginzburg & Zhelezniakov 1958; Papadopoulos & Freund1979; Melrose 1980; Krasnoselskikh et al. 2019; Tkachenko et al. 2021). Notably, F exhibits a strongly structured spectral appearance, while the H emission is significantly more "diffuse" and may occasionally exhibit intensity variations and weak structuring.

The starting frequencies of the F and H components are different for each burst. Generally, the H component is first seen more often at higher frequencies (>15 MHz), whereas F is first seen starting slightly lower. In the example burst shown in Figure 1(b), the H component starts at around 19 MHz, while the F component exhibits fragmentation and is observed first near 15 MHz. The F component is observed continuing into low frequencies (<1 MHz), while H is observed less at low frequencies. This may be partly due to the domination of QTN close to the local plasma frequency f_p (the spectral tail extends beyond f_p depending on the electron density/temperature; Zaslavsky et al. 2011; Liu et al. 2023), which ranged between ∼400 kHz and ∼1 MHz, on average, between the first and 10th CEs. For reference, the f_p at a spacecraft located at 1 au is ∼20 kHz.

The very high fluxes of the background noise close to the plasma frequency may explain why most type III bursts end around 1 MHz as their signal gets lost in the exceedingly dominant QTN and it is tail. However, since f_H is emitted at close to twice f_F, it is expected that the H component corresponding to the F component emitted at 10 MHz would be at 20 MHz and is therefore shifted accordingly. This shifting procedure causes some points corresponding to H to fall below the average background noise.

In Figure 1(b), we provide an illustration of a typical type III radio burst, showcasing the primary spectral identification of F–H pairs and their simultaneous occurrence at f_p and $2f_p$. To study F–H pairs similar to the one in Figure 1(b), we analyzed both time and frequency profiles, as depicted in Figures 1(c) and (d). By measuring the difference between the central frequencies of the F and H components, we obtained the F–H frequency ratio (f_H/f_F), which was found to be $f_H = 1.9 \pm 0.12 f_F$, close to the theoretically expected $f_H = 2f_F$ (Figure 1(e)). A slight systematic deviation from the predicted $f_H = 2f_F$ toward lower frequencies is noticeable from the trend line. Recently, Melnik et al. (2018) reported a similar deviation ($f_H = 1.87$–$1.94 f_F$) in the context of M-D bursts. Their findings are in agreement with ours. This deviation is further demonstrated in Figure 1(f), which displays the measurements of the propagation time delay between f_F and f_H. In order to obtain these measurements, the temporal deviation of the rising time of the F and H components was compared at any given time for each burst at the corresponding f_H/f_F ratio. The deviation from the theoretical prediction may stem from the distinct group velocities of radio waves emitted near f_p and those emitted around $\sim 2f_p$. The propagation delay between F and H based on observations is presented in Figure 1(f), and it is linearly dependent on frequency as $f^{-0.46\pm0.04}$ (red dashed line). In Appendix B, we propose that the physical difference in group velocities could account for a significant proportion of the time delay between the F and H emissions from the source to the observer. The integrals provided in Appendix B can accommodate any density scaling factor. Figure 1(f) demonstrates a simple $1/r^2$ approximation (depicted by the green solid line; Parker 1960), as well as a more advanced twofold Leblanc scaling (depicted by the black solid line; Leblanc et al. 1998). The delay estimation derived from the twofold Leblanc model aligns well with the observations, underscoring its strong dependence on the radial evolution of the electron density profile.

Figure 1(g) presents the peak intensity of both F and H components as a function of frequency. We note that this is the first such comparison of the two emission components in the H-K wavelengths. To make a one-to-one comparison of the F and H intensities, we shifted the points representing H to the frequency of F (i.e., $f_H/2$). The results indicate that the peak intensity of the F emission increases rapidly toward 5–2 MHz, peaking at ∼3 MHz and then slowly declining toward low frequencies (<1 MHz). Previous studies (e.g., Weber et al. 1977) have reported on the radio power peaking close to 1 MHz. A statistical trend of the mean values can be established using a piecewise fitting with two power laws,[8] one with a spectral index, $f^{-1.9\pm0.32}$, at high frequencies (19.2–2 MHz) and a flatter $f^{0.38\pm0.23}$ at low frequencies (2.5–0.75 MHz). Meanwhile, H shows a systematic increase toward low frequencies and can be fit with a single power law with a spectral index of $f^{-0.68\pm0.15}$. It is also evident from the standard deviations that F shows strong intensity variations at all frequencies and therefore presents a large spread of values compared to H. Figure 1(g) demonstrates that the two components have comparable peak intensities at high (<10 MHz) and low (<1 MHz) frequency.

To have an estimate of the physical characteristics of the exciter, we measured the drift rates of F and H at peak intensity and considered the drift rates of the half-power rising and falling as the standard deviation. We then assumed a twofold Leblanc electron density model (Leblanc et al. 1998), which is often considered for H-K radio bursts (Jebaraj et al. 2020). This analysis yielded an average exciter speed of $0.15c \pm 0.05c$ for F and $0.14c \pm 0.06c$ for H. The exciter speed of the example burst presented in Figure 1(b) is $0.16c \pm 0.05c$ for F and $0.15c \pm 0.06c$ for H. Such speeds are considered nominal type III exciter speeds (Dulk et al. 1984). It should be noted that the

[8] The piecewise laws were obtained to be continuous, and the limits are chosen based on the transition at which the fit parameters change significantly.

choice of electron density model introduces an error; therefore, this result should be treated as only a first-order approximation. The F–H pairs are produced by the same exciter, and as a result, the measured spectral drifts are generally assumed to be identical. The difference in spectral drift of about $0.01c$ could possibly be attributed to a combination of propagation effects (Appendix B) and different emission mechanisms.

In addition to the spectral characteristics reported above, we have also analyzed the bandwidth (df/f) of the F–H components and the asymmetry of the type III time profiles (τ_f/τ_r, where τ_f is the falling time, and τ_r is the rising time).

3.1. Bandwidth

The bandwidth of the type III burst at any given time instance is calculated as the frequency difference (df) between the half-power maxima (Figure 1(d)). The relative bandwidth is then calculated by dividing df by the central frequency f. Since f_H equals $2f_F$, the H emission is shifted to f_F for a one-to-one comparison, and the results are presented in Figure 1(h). The result indicates that the peak relative bandwidths of both F and H are found in a similar range of frequencies. Figure 1(h) also shows that the relative bandwidth of the H component systematically decreases with decreasing frequency. This may be attributed to the lower intensity of H and the increasing background noise (Figure 1(g)), which makes it difficult to accurately measure the true bandwidth using just the half-power maxima.

Figure 1(h) shows that the relative bandwidth of F can be between 20% and 65% of their central frequency. Smaller bandwidths (20%–40%) are found close to the starting frequencies (13–8 MHz), after which they grow rapidly toward 6–2.5 MHz, where the average bandwidth is about 45%–60%. The bandwidth does not grow as much below 2.5 MHz and remains close to 50%. Measuring the bandwidth below 1 MHz might induce errors due to the steep increase in background noise (Figure 1(g)). We perform a piecewise fitting of the results using two power laws, obtaining a spectral index of $f^{-0.77\pm0.2}$ in the 19–5 MHz range and a flat $f^{0.2\pm0.15}$ for the frequencies between 6 and 0.75 MHz.

Meanwhile, the bandwidth of H ranged between 30% and 80% (Figure 1(h)). The largest bandwidths (60%–85%) were measured at frequencies of ∼13–5 MHz, which is twice the frequency range at which the largest bandwidths of F were found (∼6–2.5 MHz). Due to the constant decrease in the bandwidth, a single power law with a spectral index of $f^{0.55\pm0.17}$ fits best. The rapid increase in bandwidth may be due to the divergence of magnetic field lines at heights corresponding to the frequencies between 19 and 5 MHz.

3.2. Time Profile Asymmetry

The time profiles of type III radio bursts are intrinsically asymmetric (Aubier & Boischot 1972; Suzuki & Dulk 1985). This asymmetry can be used to estimate the two-phase evolution of the beam, namely, the growth of the instability and the damping timescales (Krasnoselskikh et al. 2019). Figure 1(c) demonstrates how the two phases can be measured; an exponentially modified Gaussian fit is used, and the peak intensity is marked as τ_{peak}. The fitting procedure for the exponentially modified Gaussian is described in detail by Gerekos et al. (2023) and can also be found in Appendix A. The values on either side of τ_{peak} are the half-power widths representing the asymmetry of the time profile, which is interpreted as being due to a result of the beam-generated Langmuir wave spectrum's evolution (Voshchepynets et al. 2015; Voshchepynets & Krasnoselskikh 2015). In this report, τ_f is distinguished from τ_d, which is the exponential decay time measured at intensities much lower than the half-power (∼10% peak intensity; Krupar et al. 2020) and is widely considered when discussing EM wave diffusion and other propagation effects (e.g., Alvarez 1973).

Figure 2 presents the different time profile characteristics and their relationship with frequency, intensity, and each other. The τ_r of F and H are shown as functions of frequency in Figure 2(a), and it is noticeable that the τ_r of F is considerably faster than that of H. The power-law trends indicate that the τ_r of F ($f^{-0.62\pm0.2}$) increases at a slightly faster rate than the τ_r of H ($f^{-0.48\pm0.08}$) with decreasing frequency. Taking into account the standard deviation of our fits, both F and H scale close to $1/\sqrt{f}$ with frequency. It is worthwhile to note that the large spread in the values of τ_r of F corresponds to the large variations in the emission intensity. While the mean τ_r scales slightly over $1/\sqrt{f}$, some individual F components may trend close to $1/f$.

Next, we compare the τ_r of F and H as a function of intensity. The τ_r of F is primarily due to the increment of the instability and growth of Langmuir waves (Krasnoselskikh et al. 2019; Jebaraj et al. 2023b). And such, it is largely dependent upon the characteristics of the beam and the density fluctuations. However, the τ_r of H is not as straightforward and is a dominated by the nonlinear times associated with the coalescence of the primary and reflected Langmuir wave. The results presented in Figure 2(b) demonstrate this, as the τ_r of F shows a large spread in values (Pearson's correlation coefficient of ∼10%), while the τ_r of H shows systematic growth with respect to intensity (Pearson's correlation coefficient of ∼60%).

Following this, we have analyzed the direct relationship between $F\tau_r$ and $H\tau_r$, which, when considering the mean, shows that $F\tau_r$ is ∼70% of $H\tau_r$. The mean spectral index of $1/f$ further corroborates the almost similar scaling laws obtained for F and H, i.e., $1/\sqrt{f}$ in Figure 2(a).

Measuring the τ_r of both the F and H components at decahectometer wavelengths (19.2–1 MHz) is mostly straightforward, except at the lower frequencies, where the τ_f of F may become convoluted with the τ_r of H. There are three limiting factors when measuring τ_f, namely, the temporal resolution, increasing background noise, and expected increase in τ_f with decreasing frequency. The first one is a technical issue, while the second one is a consequence of the increased plasma density during CEs, which affects the time profile of both F and H. The final factor is a physical issue arising due to the increase in the τ_f of F becoming increasingly convoluted with the time profile of H even at higher frequencies. Nevertheless, it is still possible to measure the τ_f (half-power width of the falling time from τ_{peak}) for a limited number of cases. Bearing this in mind, we have measured the τ_f of F and H whenever possible. We have not measured the exponential decay (τ_d; Krupar et al. 2020) due to the aforementioned reasons, which are further enhanced, making it difficult to identify the τ_d of F.

Figure 2(b) shows the results of measuring the τ_f of the F and H components. We find a linear trend with respect to frequency in the case of both F and H. Similar to τ_r, the large standard deviation in the measurements of F is due to the spectral

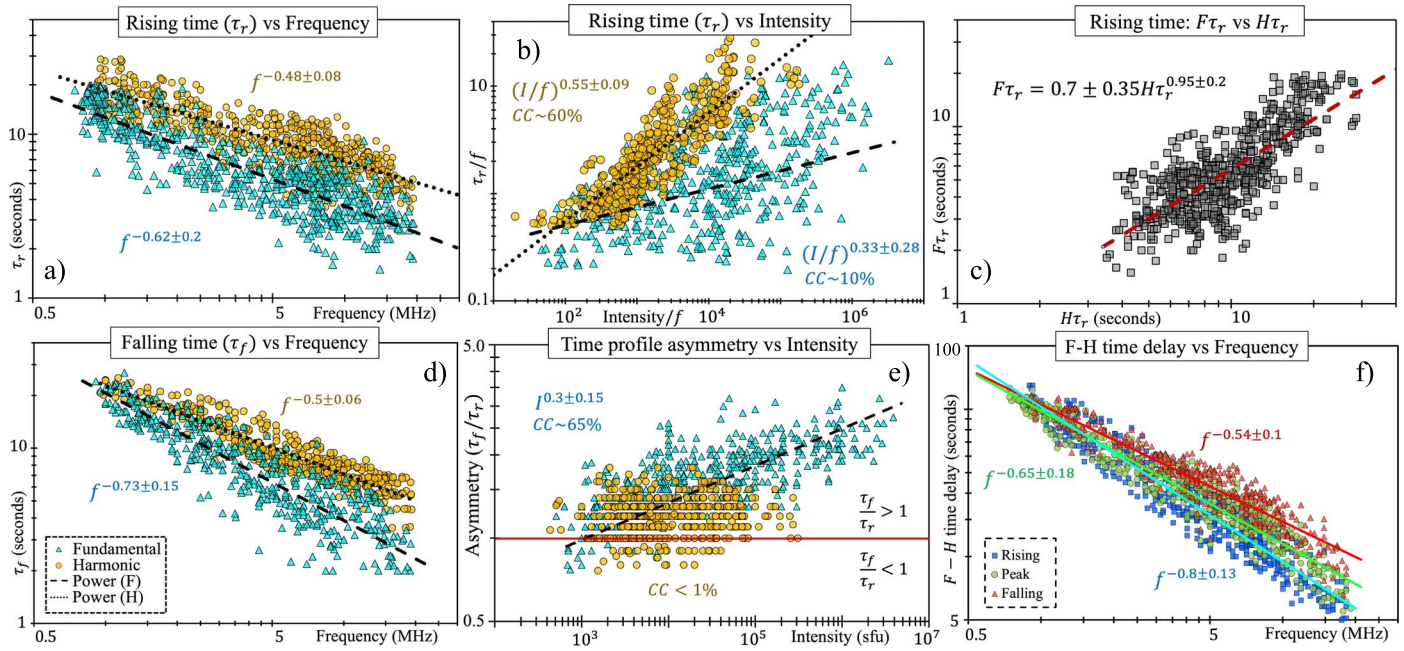

Figure 2. Time profile characteristics of the 31 type III F–H pairs. Shown is the rising time of F (blue triangles) and H (yellow circles) as a function of frequency in panel (a) and intensity in panel (b). The one-to-one relationship between the rising times of F and H is shown in panel (c). The falling time of F and H as a function of frequency is presented in panel (d), while the time profile asymmetry (τ_f/τ_r) as a function of intensity is shown in panel (e). The time delay between the F and H components at the rising and falling phases (at half-power) and peak power as a function of frequency is shown in panel (f).

structuring. Meanwhile, the standard deviation for the measurements of H is relatively small. The linear trend is fitted using a power law with a spectral index of $f^{-0.5\pm0.06}$, which is similar to the τ_r of H. In the case of F, the fitted power law has a spectral index of $f^{-0.73\pm0.15}$. Considering only the mean, the scaling law for the τ_f of F can simply be considered to be $1/f^{3/4}$.

As demonstrated in Figure 2(b), the presence of strong intensity variations in the F emission can result in a drastic spread in rising time. Similarly, the relationship between τ_r and τ_f cannot be fully understood without taking into account the intensity of the emission. Therefore, we investigated the change in τ_f/τ_r as a function of intensity. Figure 2(e) presents this result, and the first thing to note is that >80% of the time profiles were asymmetric. The sense of asymmetry was where τ_f was larger than τ_r (i.e., $\tau_f/\tau_r > 1$). The remaining time profiles were classified into two categories: those where τ_r was greater than τ_f (i.e., $\tau_f/\tau_r < 1$), and those where τ_r and τ_f were equal, resulting in perfect symmetry (i.e., $\tau_f/\tau_r = 1$).

If we were to compare the symmetry of F and H separately, the time profiles of the F components would be predominantly in the $\tau_f/\tau_r > 1$ regime and sensitive to the emission intensity. This is demonstrated further by the presence of the $\sim\tau_f/\tau_r = 1$ and $\tau_f/\tau_r < 1$ regimes when the intensity was low. Statistically, a linear trend with a Pearson's correlation coefficient of ∼65% was found for the time profiles of F components. Meanwhile, the results of the H component presented in Figure 2(a) indicated no obvious relationship between the intensity and the symmetry (Pearson's correlation coefficient of <1%). The H component was also likely to be far more symmetric ($\tau_f/\tau_r = 1$) in comparison to the F component. In terms of asymmetry, we noted only minor asymmetry, which was irrespective of the emission intensity.

This result was different from the one obtained in Figure 2(b), where no significant correlation was found between the emission intensity and the rising time. When considering the falling time as well, the asymmetry of the F emission was correlated strongly with the variations in intensity.

Additionally, in Figure 2(f), we report for the first time the time delay between the F–H pairs at discrete frequencies. As a result of emissions from distinct regions, F and H emissions emitted at a specific frequency are anticipated to become more divergent as the frequency decreases. This divergence offers a potential means of measuring the speed of the exciter. This separation between F–H pairs has not been reported previously due to the poor temporal resolution of H-K observations. In Figure 2(f), we demonstrate that it is possible to measure the time delay between the rising (blue squares), peak (green diamonds), and falling (red triangles) of the frequency–time profile of the F–H pairs. As their emission regions (f_p and $2f_p$) become increasingly separated with decreasing frequency, so too does the time difference between different parts of the F–H pairs. The results indicate that there is a systematically increasing delay between them, which can be best fitted using power laws with spectral indices: $f^{-0.8\pm0.13}$ (rising), $f^{-0.65\pm0.18}$ (peak), and $f^{-0.54\pm0.1}$ (falling). The time difference between the rising and falling phases is measured by taking the half-power maxima of the F–H pairs (shown in Figure 1(b)). By utilizing a simple density model (twofold; Leblanc et al. 1998), we derived $0.2c(\pm0.026c)$, $0.16c(\pm0.03c)$, and $0.11c(\pm0.018c)$ for the rising, peak, and falling times, respectively (Figure 2(f)). This finding supports the estimate we presented in Section 3.

4. Polarization

When the F and H components of a radio burst are clearly distinguishable, we can also study the polarization properties of the individual components. While a detailed description of the polarization properties is beyond the scope of this letter, we can

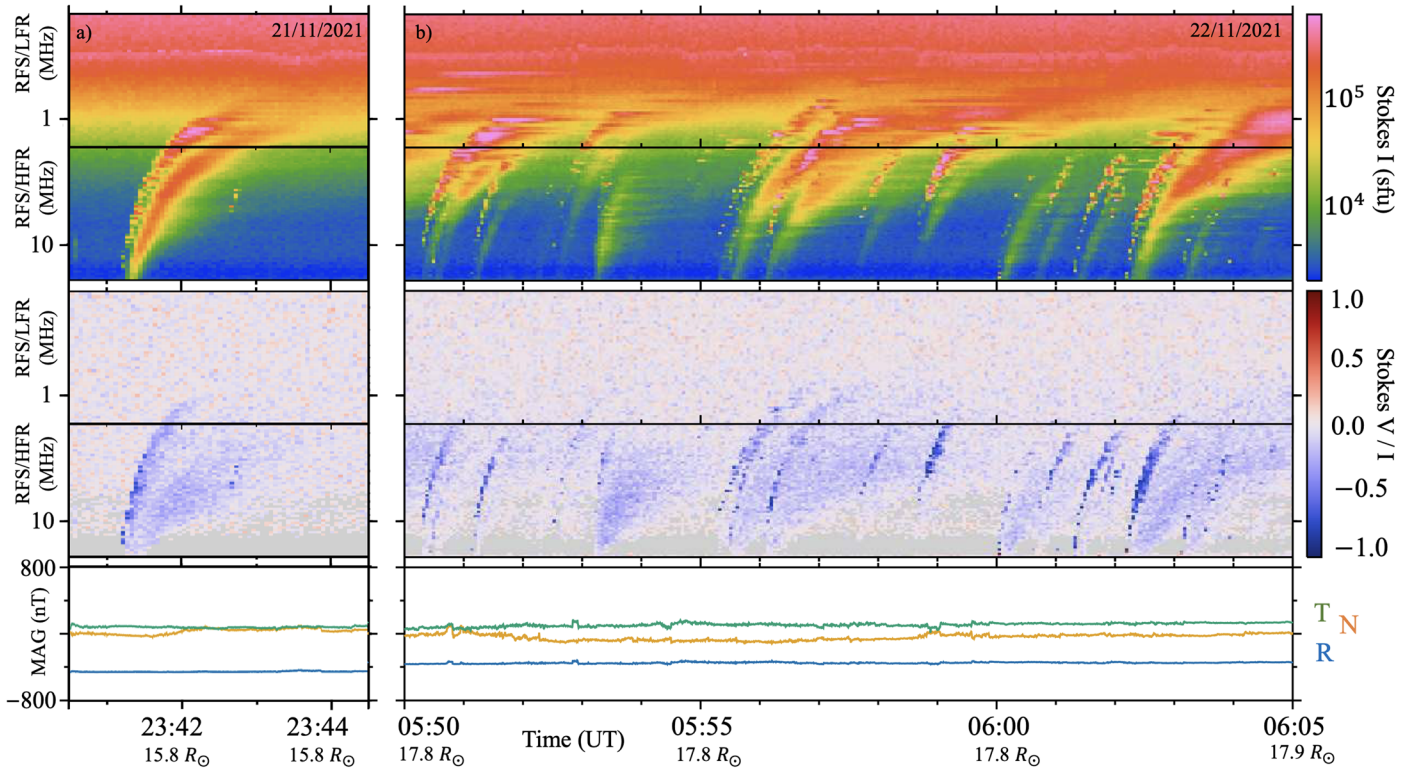

Figure 3. Examples with polarization. The top panels show the Stokes intensity I parameter from HFR and LFR for the same example type III burst shown in Figure 1(a) and a longer 15 minute time period on 2021 November 22 (panel (b)). The middle panels show the corresponding relative Stokes polarization V/I. Separate polarized components are visible for both F and H components of the burst. The bottom panels show the magnetic field in RTN coordinates, with the field dominated by a negative (sunward) radial component.

make a few initial observations using the same examples presented in Figures 1(a) and (b). For these example bursts, we calculate the Stokes parameters as in Pulupa et al. (2020). The polarization measurements provide additional confirmation that the observed bursts are indeed F–H pairs.

For F–H type IIIs where polarization is evident, the properties are broadly consistent with those described in Dulk & Suzuki (1980) from ground-based observations at 24–220 MHz.

The degree of polarization (DOP), represented using the ratio of Stokes V to I parameters, is strongest near the leading edge of the F component and significantly weaker for the H component. In the example in Figure 3(a), the F Stokes V/I reaches a maximum of ∼0.7, while the V/I for the H component is 0.2–0.3. As is the case with the intensity, the circular polarization for the F component is highly variable, while the H component is smoother. Figure 3(b) presents a longer, 15 minute duration during the same CE on 2021 November 22. A number of type III F–H pairs are distinguished, and the Stokes V/I of F reaches or exceeds ∼0.5 for all cases, with some even a reaching maximum of close to ∼1.0. As with the example presented in Figure 3(a), the H component shows substantially lower DOP, ∼0.3, on average. The F component also exhibits strong variations, while the H is diffuse. It is also worthwhile to note that the polarization is substantially higher for fine structures within F emission.

The high DOP in the measurements is attributed to the angle between the magnetic field at the emission source and the direction to the spacecraft. Consequently, it is not surprising that the DOP varies across different source regions, as demonstrated by the groups of type III bursts examined in a recent study (Dresing et al. 2023). Another study by Pulupa et al. (2020) analyzed a type III radio burst storm during the PSP's second CE and similarly found a high DOP. Additionally, prior studies based on observations at 1 au (Reiner et al. 2007) reported much smaller DOP values and were unable to distinguish between F and H. The polarization measurements presented here unequivocally indicate that the observed bursts are F–H pairs.

The sense of the circularly polarized emission is always the same between the F and H components and is determined by the direction of the magnetic field at the source region. For the F component, which is emitted near the plasma frequency f_p, the x-mode radiation produced at the source region has a frequency below f_p and cannot propagate to the observer. Therefore, the observed emission should be in the o mode, which is left-hand circularly polarized when the radial component of the source region magnetic field $B_r > 0$ and right-hand circularly polarized (RHC) when $B_r < 0$. Although the sense of polarized F emission is determined by the direction of the field, it is not well understood what controls the DOP, i.e., why emission that is restricted to one mode is not 100% polarized. Reflection off of regions with enhanced density (Melrose 2006) can result in depolarization, and simulations that include the effects of density variation (Kim et al. 2007, 2008) indicate that it is possible to produce emission in the x and o modes simultaneously. Such a scenario may also explain the high polarization of the fine structures within F emission where density inhomogeneities are relatively low

(Jebaraj et al. 2023b). The general decrease in polarization observed below 1.5 MHz may be attributed to plasma inhomogeneities between the source and the observer, the aforementioned mode coupling between the x and o modes, and the directivity of emission with respect to the observer. For the H component, the sense of polarization matches that of the F component. The degree of H polarization is related to the ratio of the cyclotron frequency f_c to f_p in the source region (Dulk & Suzuki 1980).

The proximity of PSP to the source of the emission and the fact that the magnetic field trends more radial in the inner heliosphere (Badman et al. 2021) allow us to directly compare the sense of polarization using the in situ magnetic field data. In Figure 3, we can confirm that the RHC sense of polarization for F and H matches the negative sign of B_r.

5. Conclusions

In this letter, we have reported for the first time clearly distinguishable F–H pairs among type III radio bursts observed in the hectokilometric (H-K) wavelengths. We attribute this finding to the close proximity of the observer to the source and the enhanced time and frequency resolution of the FIELDS/RFS receivers on board the Parker Solar Probe (PSP). The main findings of this letter are as follows.

1. We found that a majority (more than 70%) of the type III radio bursts observed during PSP CEs 6–10 are F–H pairs. We also found that their occurrence rate is slightly higher during storm periods (78%).
2. The morphology of the F emission exhibits strong structuring, while the H emission appears diffuse in both Stokes I and V, resembling the type IIIb–type III pairs observed in metric–decametric wavelengths.
3. There is a systematic delay in propagation between the F and H emission that increases with decreasing frequency and offsets the theoretically expected $f_H = 2f_F$ to $f_H = 1.9 \pm 0.12 f_F$. We have demonstrated that this is due to the difference in group velocity of the F and H.
4. We found that the time profile asymmetry of F is well correlated to the intensity of the emission. However, the H emission shows no such correlation.
5. Our results indicate that the rising time of F is consistently faster than that of H regardless of intensity. The variations of the rising time of F emission are also strongly associated with its intensity; i.e., the more intense the emission, the faster the rise.
6. The F emission is highly polarized (~50%, on average, in the 19–1.5 MHz frequency range), with some bursts showing close to 100% polarization. Meanwhile, the H emission is weakly polarized (~30% or lower, on average). The high polarization of F indicates that it is generated predominantly as o-mode radiation, while H is a mix of both x- and o-mode radiation.
7. The duration parameters (τ_r and τ_f) of the H scale linearly with frequency at a rate of $1/\sqrt{f}$, while those of the F exhibit complexity due to strong intensity variations. Specifically, τ_r scales close to $1/\sqrt{f}$, while τ_f scales as $1/f^{3/4}$.

The observational evidence and statistical results presented in this letter on the observational characteristics of the F and H emission components near the source offer new avenues for exploration in the H-K wavelengths. Observing radio bursts in close proximity to their source allows us to deepen our understanding of F plasma processes and the generation of radio emission in inhomogeneous plasma. Aside from the F aspects of the beam–plasma system, our study builds upon previous research conducted by Krupar et al. (2020) and offers valuable enhancements for probing the evolution of density turbulence in the coronal and solar wind plasma. The impact of multiple vantage point radio observations on the analysis of solar energetic particle transport continues to grow rapidly. Type III bursts serve as a powerful tool for comprehending the propagation path of the energetic particles and subsequent plasma conditions (e.g., Dresing et al. 2023; Jebaraj et al. 2023a). Consequently, distinguishing between F and H aids in refining the techniques used to pinpoint the source of type III bursts and improve source propagation estimation (direction finding; Lecacheux 1978). Furthermore, this discovery greatly contributes to the long-standing challenge of distinguishing between radio wave generation and propagation (Arzner & Magun 1999, and references therein). Specifically, the exponential decay provides pivotal insights into the processes influencing radio waves. Due to the lack of radio imaging in the H-K wavelength range, distinguishing the characteristics of the F–H time profiles is crucial.

In forthcoming publications, we will also progress the state of the art by addressing the generation of both the F and H emission that has been predicted by the probabilistic model of beam–plasma interactions (Tkachenko et al. 2021; Krafft & Savoini 2022) using experimental data from PSP. Finally, coordinated observations made with the PSP during its CEs in conjunction with the Radio Plasma Waves (Maksimovic et al. 2020) instrument on board the Solar Orbiter (SolO; Müller et al. 2013) may offer additional opportunities to understand multiscale plasma processes in the high corona and interplanetary space. A likely avenue for future exploration is a survey of type III radio bursts using PSP and SolO for which local Langmuir waves are observed. A similar approach to Reiner & MacDowall (2019) would make it possible to distinguish F–H pairs at lower frequencies (i.e., <400 kHz). At such frequencies, propagation effects and the effect of a larger spatial extent of the source may result in emission from a wider range of frequencies simultaneously, making the peak frequencies less pronounced.

Acknowledgments

This research was supported by the International Space Science Institute (ISSI) in Bern through ISSI International Team project No. 557, Beam-Plasma Interaction in the Solar Wind and the Generation of Type III Radio Bursts. I.C.J. acknowledges support from ISSI's visiting scientist program. The Parker Solar Probe was designed, built, and is now operated by the Johns Hopkins Applied Physics Laboratory as part of NASA's Living with a Star (LWS) program (contract NNN06AA01C). Support from the LWS management and technical team has played a critical role in the success of the Parker Solar Probe mission. V.K. acknowledges financial support from CNES through grants, "Parker Solar Probe," and "Solar Orbiter," and by NASA grant 80NSSC20K0697. J.M. acknowledges funding by the BRAIN-be project SWiM (Solar Wind Modeling with EUHFORIA for the new heliospheric missions).

Appendix A
Exponentially Modified Gaussian

The type III time profiles that exhibit a rapid Gaussian-like rise and an exponential decay were fitted using a five-parameter function known as the exponentially modified Gaussian function. This function, which was also used in Gerekos et al. (2023), is expressed as

$$g(a,\, b,\, \mu,\, \sigma,\, \lambda;\, x) = a\frac{\lambda}{2}\exp\left\{\frac{\lambda}{2}(2\mu + \lambda\sigma^2 - 2x)\right\} \times \left(1 - \mathrm{erf}\left\{\frac{\mu + \lambda\sigma^2 - x}{\sqrt{2}\,\sigma}\right\}\right) + b. \tag{A1}$$

Here the parameters have specific roles. The parameter a scales the overall magnitude of the burst, while b represents its base level, i.e., the pre-event background. The mean (μ) and variance (σ^2) determine the Gaussian portion of the function. Lastly, the decay rate (λ) controls the exponential decay part. The error function (erf(z)) is defined as $2(\pi)^{-1/2}\int_0^z e^{-t^2}\mathrm{d}t$. The values on either side of the τ_{peak} are the half-power widths representing the asymmetry of the time profile, i.e., the rising (τ_r) and falling (τ_f) times.

We perform separate fits for both F and H bursts and then combine them at the intersection point where the goodness of fit typically deviates from the >95% level. Time profiles that had a goodness below the optimal 95% level prior to the intersection are discarded. Additionally, time profiles where the intersection occurs at or before the half-maximum level are also discarded. For the H bursts, we assume the pre-event background or base level to be the same as that of the F bursts. As a result, the parameter b remains constant for both F and H at each frequency.

Appendix B
Propagation Delay between F and H Emission

The F and H emission at any given moment are emitted at different frequencies and therefore propagate with different group velocities. This physical effect is evaluated analytically in this section.

Let us evaluate the "time of flight" of the EM wave between the source region where the generation occurs and the observer.

For this purpose, we use the Hamiltonian description:

$$\frac{d\boldsymbol{k}}{dt} = -\nabla\omega, \tag{B1}$$

$$\frac{d\boldsymbol{r}}{dt} = \boldsymbol{V}_{\mathrm{gr}} = \frac{\partial\omega}{\partial\boldsymbol{k}}. \tag{B2}$$

Here V_{gr} is the group velocity, and ω is the frequency in radians per second and is related to f as $\frac{\omega}{2\pi}$.

Let us formulate the problem in a simplified version. The wave is generated at some source point, which we shall notify by index S, and propagates along the radius, and the plasma density depends only on the radial distance. Let the radial dependence be described by an expression,

$$n(R) = n_S\left(\frac{R_S}{R}\right)^{\alpha}$$

$$\frac{\omega_p(R)}{\omega_{pS}} = \left(\frac{R_S}{R}\right)^{\alpha/2},\ R = R_S\left(\frac{\omega_{pS}}{\omega_p(R)}\right)^{2/\alpha}. \tag{B3}$$

Then, a simple calculation allows one to obtain the following set of equations:

$$\begin{aligned}
\frac{d\boldsymbol{k}}{dt} &= -\nabla\omega_p \\
\boldsymbol{V}_{\mathrm{gr}} &= \omega_p\frac{\boldsymbol{k}c^2}{\omega_p^2\sqrt{1 + \frac{k^2c^2}{\omega_p^2}}} = \frac{\boldsymbol{k}c}{\omega}c \\
\frac{d\boldsymbol{V}_{\mathrm{gr}}}{dt} &= -\frac{c^2}{\omega}\nabla\omega_p \\
\frac{dV_{\mathrm{gr}}}{dt} &= \frac{\alpha c^2 R_S^{\alpha}}{\omega R^{\alpha+1}}\omega_{p_S}, \\
\frac{dR}{dt} &= \boldsymbol{V}_{\mathrm{gr}} \\
\frac{d^2R}{dt^2} &= \frac{\alpha c^2 R_S^{\alpha}}{\omega R^{\alpha+1}}\omega_{p_S} \\
\frac{dR}{dt}\frac{d^2R}{dt^2} &= \frac{dR}{dt}\frac{\alpha c^2 R_S^{\alpha}}{\omega R^{\alpha+1}}\omega_{p_S}
\end{aligned} \tag{B4}$$

$$V_{\mathrm{gr}}^2 - V_{grS}^2 = \frac{2c^2}{\omega}\omega_{p_S}\left[1 - \left(\frac{R_S}{R}\right)^{\alpha}\right], \tag{B5}$$

$$V_{\mathrm{gr}}^2 = \left\{V_{grS}^2 + \frac{2c^2}{\omega}\omega_{p_S}\left[1 - \left(\frac{R_S}{R}\right)^{\alpha}\right]\right\}. \tag{B6}$$

Knowing the group velocity allows us to evaluate the time of flight,

$$\begin{aligned}
T &= \int_{R_S}^{R}\frac{dR}{\left[V_{grS}^2 + \frac{2c^2}{\omega}\omega_{pS}\left(1 - \left(\frac{R_S}{R}\right)^{\alpha}\right)^{1/2}\right]} \\
&= R_S\int_1^{R/R_S}\frac{y^{\alpha/2}dy}{\left[\left(V_{grS}^2 + \frac{2c^2}{\omega}\omega_{pS}\right)y^{\alpha} - \frac{2c^2}{\omega}\omega_{pS}\right]^{1/2}} \\
T &= \left(\frac{\omega}{2\omega_{pS}}\right)^{1/2}\frac{R_S}{c}\int_1^{R/R_S}\frac{y^{\alpha/2}dy}{\left[\left(\frac{\omega V_{grS}^2}{2c^2\omega_{pS}} + 1\right)y^{\alpha} - 1\right]^{1/2}} \\
&= \left(\frac{\omega}{2\omega_{pS}}\right)^{1/2}\frac{R_S}{c}\int_1^{R/R_S}\frac{y^{\alpha/2}dy}{[Qy^{\alpha} - 1]^{1/2}},
\end{aligned} \tag{B7}$$

where $Q = \left(\frac{\omega V_{grS}^2}{2\omega_{pS}c^2} + 1\right)$, and $y = \frac{R}{R_S}$. This time can be evaluated for a wave generated at a F frequency and its H. Let us first evaluate the parameter Q for the F frequency.

In order to do that, let us analyze the relations between frequencies and k-vectors. For the F frequency, the Langmuir wave frequency is written as

$$\omega_{\mathrm{L}} = \omega_p\left(1 + \frac{3}{2}k_{\mathrm{L}}^2\lambda_D^2\right) = \omega_{tF} = \omega_p\left(1 + \frac{1}{2}\frac{k_t^2c^2}{\omega_p^2}\right). \tag{B8}$$

Here the subscript t indicates a transverse wave (EM wave) generated with the same frequency as the primary Langmuir wave. So, $k_{\rm L}$ is the k-vector of the primarily generated Langmuir wave, which is given by $k_{\rm L} = \frac{\omega_p}{V_b}$, and then $k_{tF} = \sqrt{3}\,k_{\rm L}\frac{\lambda_D\omega_p}{c} = \sqrt{3}\,\frac{\omega_p}{V_b}\frac{v_T}{c}$ is the vector of the EM wave. Using this vector, we can find the group velocity for the F frequency as

$$V_{grSF} = \frac{k_{tF}c^2}{\omega_p\left(1+\frac{k_{tF}^2c^2}{\omega_p^2}\right)^{1/2}} = \frac{k_{tF}c}{\omega}c = \sqrt{3}\frac{v_T}{V_b}c. \tag{B9}$$

Therefore, the parameter Q for F emission is equal to

$$Q_F = \left(\frac{3v_T^2}{2V_b^2}+1\right). \tag{B10}$$

The time of flight for the wave generated at a F frequency under the condition that it propagates radially from the source to the observer without small-angle scattering is evaluated to be

$$\begin{aligned} T_F &= \frac{R_S}{\alpha c}\frac{\sqrt{2}}{2}\int_1^{R/R_S}\frac{y^{\alpha/2}dy}{(Q_F y^\alpha - 1)^{1/2}} \\ &= \frac{R}{\alpha c}\left(\frac{\omega_{pL}}{\omega}\right)^{2/\alpha}\frac{\sqrt{2}}{2}\int_1^{R/R_S}\frac{y^{\alpha/2}dy}{(Q_F y^\alpha - 1)^{1/2}}. \end{aligned} \tag{B11}$$

Here ω_{pL} is the local plasma frequency. It is easy to make similar calculations for the H emission. The initial k-vector of the wave generated by nonlinear wave–wave interaction satisfies the following:

$$2\omega_p = \sqrt{k^2c^2+\omega_p^2}, \tag{B12}$$

$$k_{SH} = \sqrt{3}\frac{\omega}{2c}, \tag{B13}$$

$$V_{grSH} = \frac{\sqrt{3}}{2}c. \tag{B14}$$

The time of flight for the H emission can then be given as

$$\begin{aligned} T_H &= \int_{R_S}^{R}\frac{dR}{\left[V_{grSH}^2 + \frac{2c^2}{\omega}\omega_{p_S}\left(1-\left(\frac{R_S}{R}\right)^\alpha\right)^{1/2}\right]}, \\ T_H &= \int_{R_S}^{R}\frac{dR}{\left[\frac{3}{4}c^2 + c^2\left(1-\left(\frac{R_S}{R}\right)^\alpha\right)^{1/2}\right]} \\ &= \frac{R_S}{c}\int_1^{R/R_S}\frac{d(R/R_S)}{\left[\frac{7}{4}-\left(\frac{R_S}{R}\right)^\alpha\right]^{1/2}}. \end{aligned}$$

Changing variable $(R/R_S) = y$,

$$\begin{aligned} T_H &= \frac{R_S}{c}\int_1^{R/R_S}\frac{y^{\alpha/2}dy}{\left[\frac{7}{4}y^\alpha - 1\right]^{1/2}} \\ &= \frac{2R}{\sqrt{7}\,c}\left(\frac{\omega_{pL}}{\omega}\right)^{2/\alpha}\int_1^{R/R_S}\frac{y^{\alpha/2}dy}{\left(y^\alpha - \frac{4}{7}\right)^{1/2}}. \end{aligned} \tag{B15}$$

The difference of arrival times is presented by the following expression:

$$\Delta T = T_F - T_H. \tag{B16}$$

The integrals T_F and T_H can be evaluated numerically for sophisticated electron density profiles. However, as an exercise, a simple calculation for the case $\alpha = 2$ is provided here. The time difference (ΔT) may then also be presented in the form of analytic expressions. Under the assumption $R >> R_S$, one can find the following approximate expressions:

$$T_F = \frac{R}{c\sqrt{2}}\left\{\left(1-\frac{R_S}{R}\right)^{1/2} + \frac{R_S}{R}\ln\left[\left(\frac{R}{R_S}\right)^{1/2} + \left(\frac{R}{R_S}-1\right)^{1/2}\right]\right\},$$

and

$$T_H = \frac{2R}{c\sqrt{7}}\left[1+\frac{4}{7}\frac{R_S}{R}\ln\left(\frac{7R}{4R_S}\right)\right].$$

Rough evaluation gives the following:

$$\Delta T \approx 0.1\frac{R}{c}. \tag{B17}$$

ORCID iDs

Immanuel Christopher Jebaraj https://orcid.org/0000-0002-0606-7172
Vladimir Krasnoselskikh https://orcid.org/0000-0002-6809-6219
Marc Pulupa https://orcid.org/0000-0002-1573-7457
Jasmina Magdalenic https://orcid.org/0000-0003-1169-3722
Stuart D. Bale https://orcid.org/0000-0002-1989-3596

References

Alvarez, H., & Haddock, F. T. 1973, SoPh, 30, 175
Arzner, K., & Magun, A. 1999, A&A, 351, 1165
Aubier, M., & Boischot, A. 1972, A&A, 19, 343
Badman, S. T., Bale, S. D., Rouillard, A. P., et al. 2021, A&A, 650, A18
Bale, S. D., Goetz, K., Harvey, P. R., et al. 2016, SSRv, 204, 49
Chen, L., Ma, B., Wu, D., et al. 2021, ApJL, 915, L22
Dresing, N., Rodríguez-García, L., Jebaraj, I. C., et al. 2023, A&A, 674, A205
Dulk, G. A. 2000, GMS, 119, 115
Dulk, G. A., Steinberg, J. L., & Hoang, S. 1984, A&A, 141, 30
Dulk, G. A., & Suzuki, S. 1980, A&A, 88, 203
Fox, N. J., Velli, M. C., Bale, S. D., et al. 2016, SSRv, 204, 7
Gerekos, C., Steinbrügge, G., Jebaraj, I., et al. 2023, arXiv:2307.01747
Ginzburg, V. L., & Zhelezniakov, V. V. 1958, SvA, 2, 653
Jebaraj, I. C., Kouloumvakos, A., Dresing, N., et al. 2023b, A&A, 675, A27
Jebaraj, I. C., Magdalenic, J., Krasnoselskikh, V., Krupar, V., & Poedts, S. 2023b, A&A, 670, A20
Jebaraj, I. C., Magdalenic, J., Podladchikova, T., et al. 2020, A&A, 639, A56
Kellogg, P. J. 1980, ApJ, 236, 696
Kim, E.-H., Cairns, I. H., & Robinson, P. A. 2007, PhRvL, 99, 015003
Kim, E.-H., Cairns, I. H., & Robinson, P. A. 2008, PhPl, 15, 102110
Krafft, C., & Savoini, P. 2022, ApJL, 934, L28
Krasnoselskikh, V., Voshchepynets, A., & Maksimovic, M. 2019, ApJ, 879, 51
Krupar, V., Szabo, A., Maksimovic, M., et al. 2020, ApJS, 246, 57
Leblanc, Y., Dulk, G. A., & Bougeret, J.-L. 1998, SoPh, 183, 165
Lecacheux, A. 1978, A&A, 70, 701
Liu, M., Issautier, K., Moncuquet, M., et al. 2023, A&A, 674, A49
Maksimovic, M., Bale, S. D., Chust, T., et al. 2020, A&A, 642, A12
McLean, D. J., & Melrose, D. B. 1985, in Solar Radiophysics: Studies of Emission from the Sun at Metre Wavelengths, ed. D. J. McLean & N. R. Labrum (Cambridge: Cambridge Univ. Press), 237
Melnik, V. N., Brazhenko, A. I., Frantsuzenko, A. V., Dorovskyy, V. V., & Rucker, H. O. 2018, SoPh, 293, 26
Melrose, D. B. 1980, SSRv, 26, 3
Melrose, D. B. 2006, ApJ, 637, 1113
Müller, D., Marsden, R. G., St., Cyr, O. C., & Gilbert, H. R. 2013, SoPh, 285, 25
Page, B., Bassett, N., Lecacheux, A., et al. 2022, A&A, 668, A127
Papadopoulos, K., & Freund, H. P. 1979, SSRv, 24, 511
Parker, E. N. 1960, ApJ, 132, 821
Pulupa, M., Bale, S. D., Badman, S. T., et al. 2020, ApJS, 246, 49
Pulupa, M., Bale, S. D., Bonnell, J. W., et al. 2017, JGRA, 122, 2836

Reiner, M. J., Fainberg, J., Kaiser, M. L., & Bougeret, J. L. 2007, SoPh, 241, 351
Reiner, M. J., & MacDowall, R. J. 2019, SoPh, 294, 91
Robinson, P. A., & Cairns, I. H. 1998a, SoPh, 181, 363
Robinson, P. A., & Cairns, I. H. 1998b, SoPh, 181, 395
Robinson, P. A., & Cairns, I. H. 1998c, SoPh, 181, 429
Suzuki, S., & Dulk, G. A. 1985, in Solar Radiophysics: Studies of Emission from the Sun at Metre Wavelengths, ed. D. J. McLean & N. R. Labrum (Cambridge: Cambridge Univ. Press), 289
Tkachenko, A., Krasnoselskikh, V., & Voshchepynets, A. 2021, ApJ, 908, 126
Voshchepynets, A., & Krasnoselskikh, V. 2015, JGRA, 120, 139
Voshchepynets, A., Krasnoselskikh, V., Artemyev, A., & Volokitin, A. 2015, ApJ, 807, 38
Weber, R. R., Fitzenreiter, R. J., Novaco, J. C., & Fainberg, J. 1977, SoPh, 54, 431
Zaslavsky, A., Meyer-Vernet, N., Hoang, S., Maksimovic, M., & Bale, S. D. 2011, RaSc, 46, RS2008